Available online at www.sciencedirect.com
SCIENCE DIRECT
Journal of Solid State Chemistry 179 (2006) 2086–2092
JOURNAL OF SOLID STATE CHEMISTRY
www.elsevier.com/locate/jssc

Crystallographic and magnetic properties of $CaLaMnMoO_6$ double perovskite

Qisheng Lin[a], Martha Greenblatt[a,*], El'ad N. Caspi[b], Maxim Avdeev[c]

[a]*Department of Chemistry and Chemical Biology, Rutgers, The State University of New Jersey, Piscataway, NJ 08854, USA*
[b]*Physics Department, Nuclear Research Centre-Negev, P.O. Box 9001, 84190 Beer-Sheva, Israel*
[c]*Bragg Institute, ANSTO, PMB 1, Menai, NSW 2234, Australia*

Received 16 February 2006; received in revised form 21 March 2006; accepted 26 March 2006
Available online 15 May 2006

Abstract

Powder neutron diffraction studies show that $CaLaMnMoO_6$ double perovskite crystallizes in monoclinic $P2_1/n$, with $a = 5.56961(9)$, $b = 5.71514(9)$, $c = 7.9358(1)$ Å and $\beta = 90.043(1)^\circ$. Mn and Mo occupy the $2c$ and $2d$ positions, respectively, with 6.0(4)% Mn/Mo anti-site mixing. Temperature-dependent magnetic susceptibility measurements reveal that $CaLaMnMoO_6$ is ferrimagnetic, with $T_N = 92(3)$ K, below which large magnetic frustration is detected. The zero-field magnetic moment measured at 5 K is about 1.2 μ_B, comparable to that of $ALaMnMoO_6$ (A = Ba and Sr), but much lower than expected for antiparallel ordering of formally Mn^{2+} (d^5) and Mo^{5+} (d^1). Moreover, no long-range magnetic ordering is observed in neutron diffraction data down to 4 K. The magnetic frustration is discussed in the framework of nearest-neighbors next-nearest-neighbors magnetic frustration.

Keywords: $CaLaMnMoO_6$; Double perovskite; Neutron diffraction; Magnetic properties

1. Introduction

The discovery of colossal-magnetoresistance (CMR) properties at temperatures significantly above room temperature in the Sr_2FeMoO_6 double perovskite [1] stimulated the search for similar effects in related $A_2BB'O_6$ type double perovskites (where A is an alkaline-earth or rare-earth ion, and B and B' are different transition metal cations) [2–4], partly driven by the possible technological applications of these materials in magnetoelectronic devices. In general, the interesting physical properties of the new perovskites are primarily due to the electronic interactions of B-site cations. For example, when Re^{6+} (d^1) is substituted for Mo^{5+} (d^1) in Sr_2FeMoO_6, a spin-dependent tunneling-type giant magnetoresistance (MR), which subsists up to room temperature in annealed samples, is observed [2].

Recently, in our search for new d^1–d^5 magnetic double perovskites, isoelectronic with Sr_2FeMoO_6, we have reported on $ALaMnMoO_6$ (A = Sr, Ba) [5,6]. $BaLaMnMoO_6$ crystallizes in a pseudo-cubic lattice (subgroup of $Fm\bar{3}m$) with long-range ferrimagnetic ordering at low temperature and large intragrain MR [6]. The onset of the MR was found to coincide with the lower temperature anomaly in the magnetization curve at ~25 K, and not associated with the ferrimagnetic transition observed at 145 K [5]. In contrast, the $SrLaMnMoO_6$ analog was found to crystallize in monoclinic ($P2_1/n$) space group with no observed long-range magnetic order down to 4.2 K and no MR [5]. The magnetization versus field [$M(H)$] curves measured at 5 K show a hysteretic behavior, characteristic of ferrimagnetic order. However, the zero-field magnetic moments are significantly reduced for both compounds (1.4 and 1.0 μ_B for Ba- and Sr-perovskites, respectively) in comparison with the expected spin-only ferrimagnetic moment (4 μ_B), suggesting pronounced frustrations in the magnetic interactions. The origin of the reduced moment was ascribed to competition between nearest-neighbor (NN) and next-nearest-neighbor (NNN) super-exchange interactions which are dominated by the B/B'–O bond distances and the average B–O–B' angle [5].

*Corresponding author. Fax: +1 732 445 5312.
E-mail address: martha@rutchem.rutgers.edu (M. Greenblatt).

0022-4596/$ - see front matter © 2006 Elsevier Inc. All rights reserved.
doi:10.1016/j.jssc.2006.03.049

In general, shorter bond distance and/or bond angle closer to 180° leads to stronger NN super-exchange interactions. Based on the crystallographic data of ALaMnMoO$_6$ (A = Ba, Sr), it is expected that CaLaMnMoO$_6$ would exhibit the strongest magnetic frustration in the ALaMnMoO$_6$ system because of the largest misfit between the A- and B-site cations, and, similar to SrLaMnMoO$_6$, no long-range magnetic ordering at low temperature would be observed. In 1977 Nakamura and Choy [7] reported ferrimagnetic behavior for CaLaMnMoO$_6$ with a Néel temperature of T_N~100 K and an asymptotic high temperature effective moment (>400 K) of 5.7 μ_B. However, no detailed magnetic data at low temperature were given. They also found that CaLaMnMoO$_6$ crystallized in a body-centered orthorhombic symmetry, which was higher than the symmetry found for SrLaMnMoO$_6$ by neutron and X-ray diffraction data [5,8]. Moreover, no detailed atomic parameters were reported. In this paper, results of the neutron diffraction structure analysis and magnetic measurements of CaLaMnMoO$_6$ are reported.

2. Experimental

Black CaLaMnMoO$_6$ powder samples were prepared by conventional solid-state reaction under 1% H_2/Ar flow. All the starting materials $CaCO_3$ (99.99%, Alfa), La_2O_3 (99.99%, Alfa), Mn_2O_3 (99.99%, Alfa), MoO_3 (99.99%, Alfa) were preheated and the purity of each was assured by X-ray diffraction. Stoichiometric mixtures of the starting reagents were first ground, pelletized and fired at 500 °C for 6 h and 1100 °C for 12 h, then followed by firing at 1300 °C for 72 h, with two intermediate grindings.

Neutron powder diffraction data at 300, 70, 50, 30 and 4 K were collected with the high-resolution BT-1 32 detector neutron powder diffractometer at the NIST Center for Neutron Research. The sample was sealed in a vanadium container inside a dry He-filled glovebox. A closed-cycle He refrigerator was used for temperature control. A Cu (311) monochromator with 90° take-off angle, λ = 1.54030 Å, and in-pile collimation of 15 min of arc were used. Data were collected over the range of 3–168° 2θ with step length of 0.05°. The instrument is described in the NCNR website (http://www.ncnr.nist.gov/). Peak searching and indexing were performed using the Fullprof program [9]. Final structural refinements were performed using the Rietveld refinement method with the GSAS (EXPGUI) suite [10,11].

Temperature-dependent magnetic susceptibility, χ, measurements were made with a Quantum Design MPMS-XL SQUID magnetometer. The samples were zero-field cooled (ZFC) to 5 K, then a magnetic field was applied and data were collected while heating from 5 to 385 K followed by re-cooling to 5 K [field cooled (FC)]. Another ZFC–FC measurement with H = 10 kOe was performed up to 760 K. All field-dependent magnetization measurements were performed with an applied field (H) $-5\,T < H < 5\,T$.

3. Result and discussion

3.1. Crystallographic structure

The Bragg peaks of CaLaMnMoO$_6$ at room temperature were indexed with a monoclinic unit cell of dimensions $\sim\sqrt{2}a_P \times \sqrt{2}a_P \times 2a_P$ (a_P is the original perovskite cell parameter). Rietveld refinement of a model with the B-site ordered $P2_1/n$ space group was used, similar to the refined model in SrLaMnMoO$_6$ [5] (Fig. 1 and Table 1). Unconstrained refinement revealed that the thermal factor for the Mn atom at $2c$ ($0\frac{1}{2}0$) site was too large compared to the average value of other cations indicating a possible mixing with Mo. Therefore, Mn/Mo partial occupancy (with total site occupancy fixed at 100%) for the $2c$ and $2d$ sites was allowed in a subsequent refinement along with a single isotropic displacement parameter for both, which shows a value of 6.0(4)% Mn/Mo anti-site mixing. Anti-site mixing is typical for double perovskites [2,5,12].

We also attempted to refine the oxygen site occupancies, but F-ratio tests [13] showed that statistically significant improvement of Rietveld refinement quality with con-

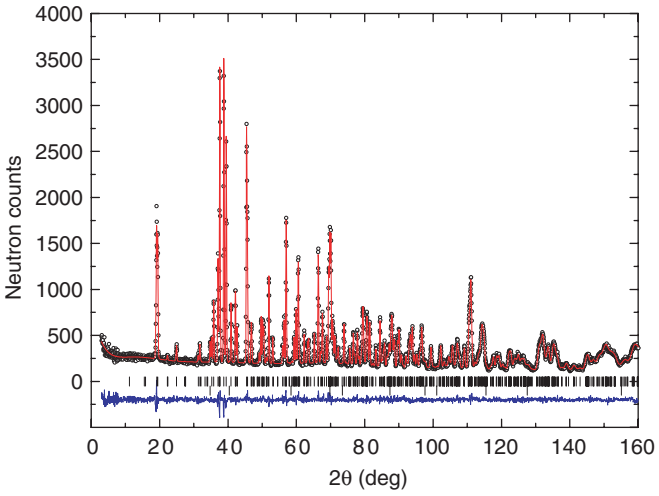

Fig. 1. Rietveld refinement of CaLaMnMoO$_6$ neutron powder diffraction data at 300 K. Experimental points are shown by circles and the calculated profile by solid line. The bottom curve is the difference pattern. The small bars indicate the angular positions of the allowed Bragg reflections of CaLaMnMoO$_6$ (upper row) and MnO (lower row).

Table 1
Crystallographic data for CaLaMnMoO$_6$

Space group	$P2_1/n$
a (Å)	5.56961(9)
b (Å)	5.71514(9)
c (Å)	7.9358(1)
β (°)	90.043(1)
R_p (%)	4.52
R_{wp} (%)	5.48
χ^2	0.974

fidence level 99% occurred only for the O1 site. Therefore, we fixed the occupancies of O2 and O3 sites to the ideal value 1 and the total oxygen content per formula unit of $CaLaMnMoO_{6-\delta}$ was found to be 5.92(2).

Attempts to refine the thermal displacement parameters anisotropically for all atoms led to some negative eigenvalues of thermal tensors. Hence, the final refinements were performed with isotropic displacement parameters for the A and B cations and with anisotropic displacement parameters for the three oxygen sites (Table 2). Since MnO was detected as an impurity, it was included as a secondary phase in the final refinement, resulting in a weight fraction of 0.96(6)% of this impurity. It is not clear from the diffraction data how the segregation of MnO is compensated exactly in the chemical composition of the perovskite phase. However, the upper limit of its effect on the stoichiometry of the material can be estimated by Eq. (1) for a hypothetical scenario of vacancy formation:

$$CaLaMnMoO_6 \rightarrow CaLaMn_{1-x}MoO_{6-x} + xMnO. \quad (1)$$

The weight fraction of MnO found from the Rietveld refinement (0.96 wt%) corresponds to $x \sim 0.058$. Although, it is not possible to confirm the value of x unambiguously from diffraction data alone, because of the high correlations of the Mn/Mo mixing and thermal parameters, this assumption is consistent with that found for the oxygen content ($\delta \sim 0.09$) discussed above. It appears that deviation of this level of the composition from the ideal one is negligible for interpreting the magnetic properties of the material. This assumption is supported by the general trends of properties observed for the series Ba–Sr–Ca as expected (vide infra).

Fig. 1 shows the fitting of the final Rietveld refinement. The refined unit cell parameters, atomic positions, thermal displacement parameters, selected bond distances and bond angles, and reliability factors are summarized in Tables 1 and 2. A $\chi^2 < 1$ in Table 1 is due to the merging of data from 32 detectors that leads to an overestimation of the uncertainty. Fig. 2 shows the structure of $CaLaMnMoO_6$ projected along the [110] direction, where the $(a^+b^-b^-)$ tilting (Glazer's notation [14]) of BO_6 octahedra is apparent.

It is useful to compare the subtle structural changes in the $ALaMnMoO_6$ (A = Ba, Sr, Ca) series [5]. Fig. 3a shows the variations of cell parameters and the Mn–O and Mo–O bond distances. With increasing effective ionic radii from Ca^{2+} to Sr^{2+} to Ba^{2+} the cell parameters a, b and c increase, as expected. The same is true for the AO_{12} polyhedra (Fig. 3b). In contrast, the average Mn–O and Mo–O bond distances, and consequently the volume of the MnO_6 and MoO_6 polyhedra slightly decrease (Fig. 3c) as the metal oxygen polyhedra distortion decreases in agreement with Shannon [15].

Another remarkable feature is the evolution of the Mn–O–Mo bond angles (ϕ), which reflect the structural distortion from ideal cubic perovskite, and, which have important implications for the interpretation of the magnetic data. The octahedral tilting angle (φ) of the MnO_6 and MoO_6 octahedra is defined as $\varphi = (180 - \phi)/2$ [3]; the calculated φ increases from 7.5° for $BaLaMnMoO_6$ to 12.5° for $SrLaMnMoO_6$ to 15.2° for $CaLaMnMoO_6$.

Table 2
Atomic coordinates, thermal displacement parameters, and selected bond distance and bond angles for $CaLaMnMoO_6$

Atom[a]	Wyck.	x	y	z	U_{iso} (Å^2)	Site occupancy (%)
La/Ca	4e	0.0105(4)	−0.0481(3)	0.2485(3)	0.0131(4)	50/50
Mn	2c	0	$\frac{1}{2}$	0	0.018(1)	100[a]
Mo	2d	$\frac{1}{2}$	0	0	0.0052(5)	100[a]
O1	4e	0.2136(4)	0.1938(5)	0.0452(3)	—	96(1)
O2	4e	0.1871(4)	0.2144(4)	0.4486(3)	—	100
O3	4e	0.5915(4)	0.0301(3)	0.2390(4)	—	100
	U_{11} (Å^2)	U_{22} (Å^2)	U_{33} (Å^2)	U_{12} (Å^2)	U_{13} (Å^2)	U_{23} (Å^2)
O1	0.011(1)	0.014(1)	0.009(1)	0.005(1)	0.0042(8)	0.0029(9)
O2	0.014(1)	0.018(1)	0.015(1)	0.0010(9)	0.0009(9)	−0.0020(9)
O3	0.015(1)	0.019(1)	0.011(1)	0.0021(7)	0.0009(9)	0.0033(10)
Bond	Distance (Å)	Bond	Distance (Å)			
Mn–O1	2.146(3)	Mo–O1	1.975(2)			
Mn–O2	2.169(2)	Mo–O2	1.979(2)			
Mn–O3	2.140(3)	Mo–O3	1.971(3)			
	Angle (°)					
Mn–O1–Mo	151.0(1)					
Mn–O2–Mo	148.3(1)					
Mn–O3–Mo	149.6(1)					

[a]There is 6.0(4)% Mn/Mo anti-site mixing.

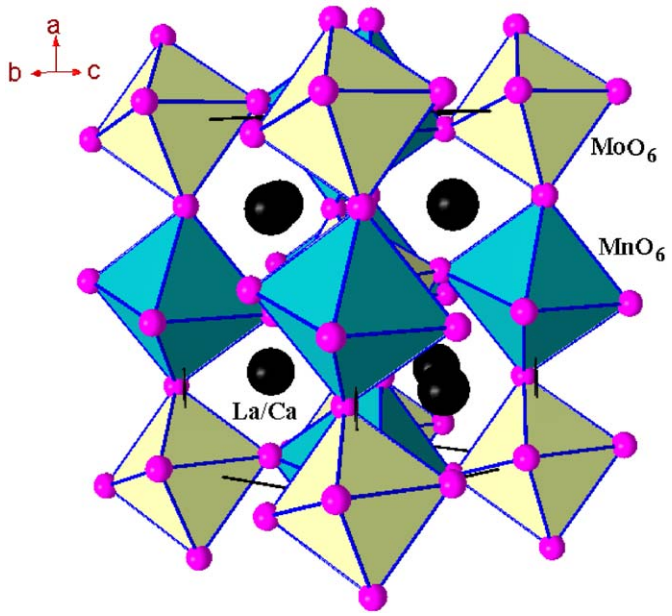

Fig. 2. Unit cell of $CaLaMnMO_6$ showing the ($a^+b^-b^-$) tilting (Glazer's notation) of MnO_6 and MoO_6 octahedra.

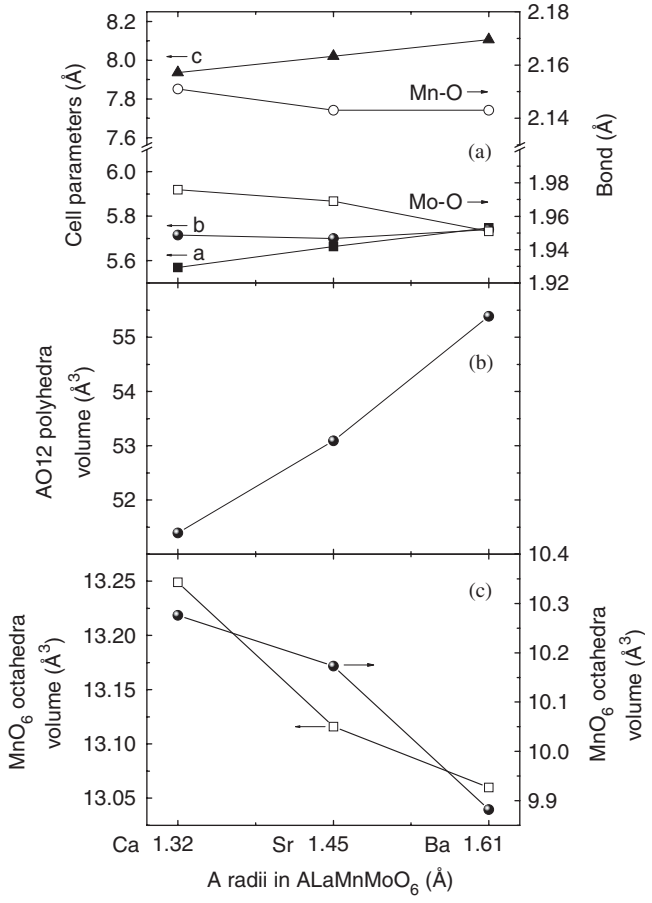

Fig. 3. Variations of cell parameters and average bond distances (a); AO_{12} polyhedra volume (b); and MnO_6 and MoO_6 octahedra volume (c) in ALaMnMoO6 (A = Ba, Sr, Ca). The data of A = Ba and Sr are taken from Ref. [5]. Errors are smaller than symbol sizes.

The unit cell parameters as a function of temperature, obtained from Rietveld analysis of the neutron data in the 4–300 K temperature range are given in Fig. 4. In addition, in the 4–70 K temperature range, the value of the unit cell angle β is constant within two standard deviations and equals ~90.075°. At 300 K it drops to 90.043(1)°. Both the temperature dependence of β, as well as the temperature dependence of a and b in the opposite sense suggest the lowering of lattice distortion in $CaLaMnMoO_6$ as the temperature increases, as expected.

3.2. Magnetic properties

The 4 K neutron diffraction pattern of $CaLaMnMoO_6$ shows no long-range magnetic ordering. The extra reflections compared to the RT pattern are associated with the previously published MnO magnetic structure [16–18]. Detailed Rietveld analysis of the 4 K neutron diffraction data is consistent with ~1 wt% antiferromagnetic MnO, and ~99 wt% of $CaLaMnMoO_6$ consistent with the 300 K neutron data. The refinement agreement factors are $R_{wp} = 4.40\%$, and $\chi^2 = 1.108$. An attempt to refine a ferromagnetic model for $CaLaMnMoO_6$ resulted in refined magnetic moment of 0 μ_B for both Mn and Mo sites.

The molar dc magnetic susceptibility of $CaLaMnMoO_6$ as a function of temperature, $\chi(T)$, shows paramagnetic behavior for $T > 92$ K, below which a sharp rise is observed, associated with ferro- or ferrimagnetic interactions (Fig. 5). The $1/\chi(T)$ plot of the ZFC data measured at a field of 10 kOe shows significant curvature in the vicinity of 200 K, typical of ferrimagnets and may be modeled with the modified Curie–Weiss law (Fig. 6; Ref. [18]):

$$\frac{1}{\chi} = \frac{T}{C} + \frac{1}{\chi_0} - \frac{\sigma}{T-\theta}, \tag{2}$$

where all parameters take their usual notations [19].

The susceptibility data was corrected for the small amount of MnO impurity. Since MnO is a *simple* Curie–Weiss paramagnet for $T > 122$ K, its susceptibility

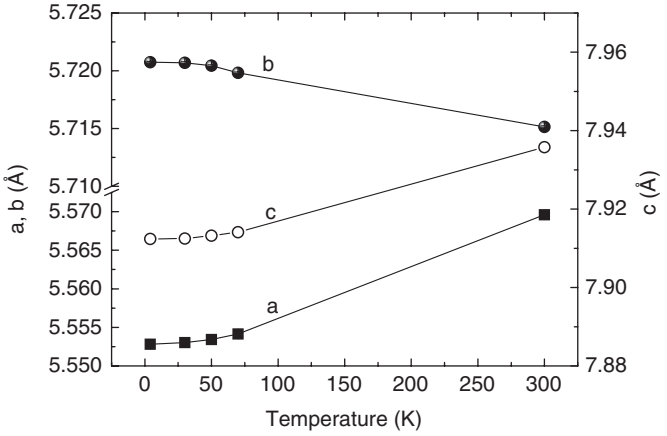

Fig. 4. $CaLaMnMoO_6$ lattice parameters a, b, and c as a function of temperature refined by Rietveld analysis of the neutron diffraction data. Errors are smaller than symbol sizes. Lines are guides to the eye.

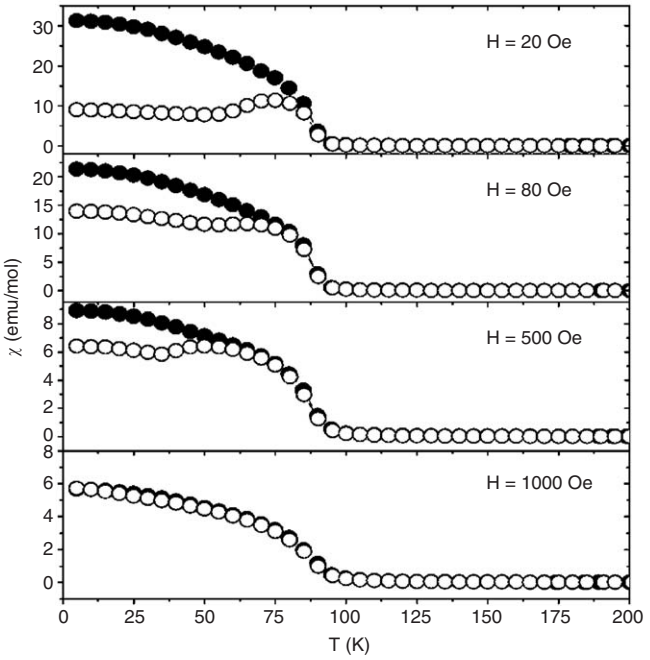

Fig. 5. Temperature-dependent magnetic susceptibility for CaLaMn MoO_6 at $H = 20$, 80, 500 and 1000 Oe with zero-field-cooled (○) and field-cooled (●) measurements (see text).

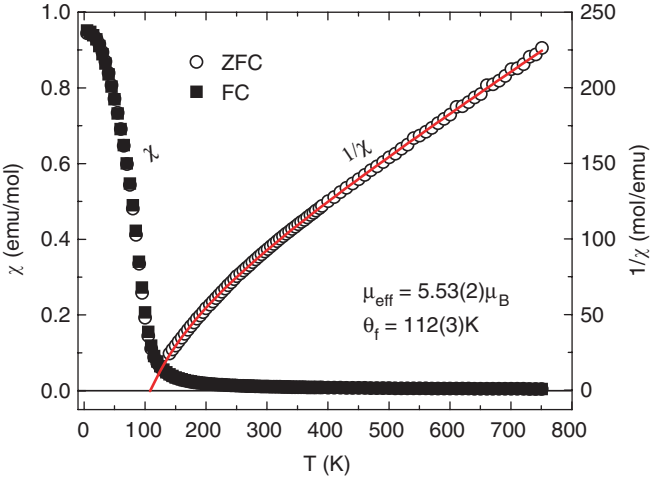

Fig. 6. Temperature-dependent magnetic susceptibility, χ and inverse susceptibility, $1/\chi$ for CaLaMnMoO_6 at $H = 10$ kOe. Solid line is a fit of the ferrimagnetic modified Curie–Weiss model to the inverse susceptibility data (see text). Zero-filed-cooled (ZFC) and field-cooled (FC) measurements are described in the text.

in this temperature region was analytically calculated using

$$\chi = \frac{C}{T-\theta_P} = \frac{\mu_{eff}^2/8}{T-\theta_P} \quad (3)$$

with $\theta_P = -610$ K, and $\mu_{eff} = 5.95\,\mu_B$ [19], and then subtracted from the $\chi(T)$ data. The corrected molar $\chi(T)$ data of CaLaMnMoO_6 were then well fitted by Eq. (2) over the temperature range of 140–760 K (Fig. 6), resulting in a ferrimagnetic Curie point of $\theta_f = 112(3)$ K and $\mu_{eff}^{modCW} = 5.53(2)\,\mu_B$. For comparison with the previously studied $BaLaMnMoO_6$ and $SrLaMnMoO_6$ [5] a fit of Eq. (3) was made to the high temperature susceptibility data in the range 400–760 K, yielding $\mu_{eff}^{CW} = 5.29(1)\,\mu_B$ and $\theta_P = -37(2)$ K for CaLaMnMoO_6; the μ_{eff}^{CW} value is very close to the ones obtained for $BaLaMnMoO_6$ [5.46(2) μ_B], and $SrLaMnMoO_6$ [5.33(2) μ_B], and is consistent with a ferrimagnetic arrangement of Mn^{2+} and Mo^{5+} spins [5].

It is worth noting that the positive values of the paramagnetic Curie temperature θ_P deduced for BaLaMn MoO_6 and $SrLaMnMoO_6$ in our previous work is probably the outcome of a simple Curie–Weiss fit (Eq. (3)) over too small of a temperature range (300–400 K). The asymptotic Curie point constant in a ferrimagnet is expected to be negative if the fit is made over a large enough temperature range [19], as was done in the present work (400–760 K).

Additional evidence for ferrimagnetism in CaLaMn MoO_6 is provided by the field dependence of magnetization ($M(H)$; Fig. 7). At temperatures 5 and 75 K an obvious hysteresis is observed in the $M(H)$ curve, whereas at 100 K it vanishes (Fig. 7 inset). This result is in excellent agreement with the 20 Oe $\chi(T)$ curve where the ZFC–FC deviation, associated with hysteretic behavior, occurs for temperatures below ~92(3) K (Fig. 5). The $M(H)$ linear plot in the high H region, when extrapolated to zero field at 5 K, yields a moment of 1.2(1) μ_B (Fig. 7). This value is much smaller than the expected 4 μ_B of the spin-only ferrimagnetic arrangement of the Mn^{2+} and Mo^{5+} ions in the magnetically ordered state, yet it is close to that of $BaLaMnMoO_6$ [1.4(1) μ_B] and $SrLaMnMoO_6$ [1.0(1) μ_B] [5].

The field dependence of the $\chi(T)$ curve reveals another intriguing feature of the magnetism in CaLaMnMoO_6 (Figs. 5 and 6). When the applied field is gradually increased from 20 to 10,000 Oe, it is clear that the transition profiles observed in the $\chi(T)$ ZFC–FC curves

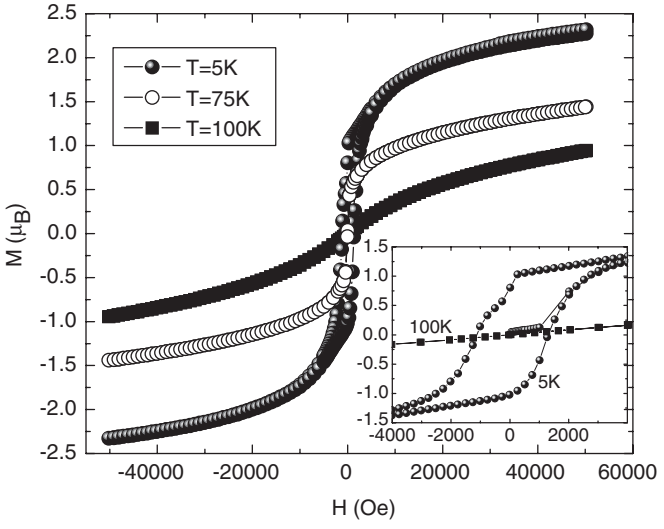

Fig. 7. Field-dependent magnetic moment, M of CaLaMnMoO_6 measured at 5, 75 and 100 K. The inset shows the enlarged hysteresis measured at 5 and 100 K.

become broader. A demonstration for this can be found in the magnitude of $(d\chi(ZFC)/dT)|_{min}$ as a function of applied field (Fig. 8). This parameter is often used as an analytical tool to identify the transition temperature in temperature-dependent susceptibility curves, since it easily identifies the temperature of largest change in the susceptibility [20]. The more negative $(d\chi(ZFC)/dT)|_{min}$ is, the sharper is the magnetic transition. In addition, the ZFC–FC divergence in the $\chi(T)$ curve appears at lower temperatures as the applied field increases (Figs. 5 and 6). These characteristics of the field dependence $\chi(T)$ curves suggest that the magnetic order is suppressed by increasing H.

Similar behavior of broadening of the transition profiles, as well as the vanishing of the ZFC–FC divergence with increasing applied magnetic field in the measurement of $\chi(T)$ were previously observed in Ba_2CoNbO_6 [21], $SrLaCuRuO_6$ [22], and $BaLaMnMoO_6$ [6] compounds. For Ba_2CoNbO_6 it was postulated that these effects are due to the suppression of the magnetic order by increasing H, and was attributed to magnetic frustration. In $SrLaCuRuO_6$ a spin-glass state was found, and magnetic frustration was argued to exist in $BaLaMnMoO_6$ [5] as well (see below).

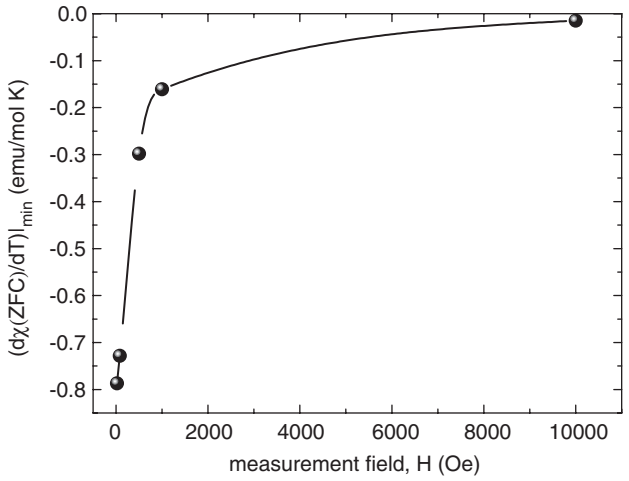

Fig. 8. Minimum value of the temperature derivative of the magnetic susceptibility, measured at zero-field-cooled, $(d\chi(ZFC)/dT)|_{min}$ as a function of applied field. Line is guide to the eye.

The suppression of magnetic order with increasing applied magnetic field, the reduced magnetic moment at zero field obtained from the $M(H)$ curves at 5 K (1.2 μ_B; Fig. 7), and the absence of long-range magnetic order in the 4 K neutron powder diffraction data, are all in agreement with the presence of strong magnetic frustration in $CaLaMnMoO_6$. Similar strong magnetic frustration is also observed in $BaLaMnMoO_6$ and $SrLaMnMoO_6$, where it was attributed to a competition between NN and NNN antiferromagnetic super-exchange interactions [5]. The crystallographic and magnetic similarities among these three compounds suggest that the same frustration mechanism is valid for $CaLaMnMoO_6$ as well.

4. Conclusion

The structure of $CaLaMnMoO_6$ double perovskite was determined by neutron powder diffraction. $CaLaMnMoO_6$ crystallized in the monoclinic space group $P2_1/n$, with $a = 5.56961(9)$, $b = 5.71514(9)$, $c = 7.9358(1)$ Å and $\beta = 90.043(1)^\circ$. Mn and Mo occupy the $2c$ and $2d$ special positions, respectively, with 6.0(4)% Mn/Mo anti-site mixing. Compared to $ALaMnMoO_6$ (A = Ba, Sr), $CaLaMnMoO_6$ has the largest octahedral distortion, as calculated from the structural data.

$CaLaMnMoO_6$ is ferrimagnetic with $T_N = 92(3)$ K and a zero-field saturated magnetic moment of 1.2(1) μ_B obtained from field-dependent magnetization measurements. This moment is comparable to that of $ALaMnMoO_6$ (A = Ba and Sr) [5], and is much reduced in comparison with the expected 4 μ_B of the spin-only ferrimagnetic arrangement of the Mn^{2+} and Mo^{5+} spins. Moreover, no long-range magnetic ordering is observed down to 4 K in the neutron diffraction data. The magnetic data observed in this work for $CaLaMnMoO_6$ is consistent with the presence of magnetic frustration, and in the $ALaMnMoO_6$ family of compounds in general.

Furthermore, close inspection of the A = Ca magnetic properties in comparison to those of A = Ba and Sr ([5]; Table 3 and Fig. 3) suggests that the strength of the frustration is largest for A = Sr and smallest for A = Ba, with A = Ca of relatively intermediate magnetic frustration, albeit with the largest crystallographic distortion. In the framework of the previously suggested NN–NNN

Table 3
Comparison of $ALaMnMoO_6$ magnetic properties for A = Ca, Sr, Ba

$ALaMnMoO_6$	ZFC–FC deviation at $H = 100$ Oe[a] (K)	$M(H)$ ($H = 0$; $T = 5$ K) (μ_B)	Long-range magnetic order	⟨Mn–O–Mo⟩ (°)	Ref.
Ca	80(5)	1.2(1)	Not observed	149.6(2)	Present
Sr	25(2)	1.0(1)	Not observed	155.1(3)	[5]
Ba	120(5)	1.4(1)	For $T < 80(10)$ K	165(1)	[5]

FC(ZFC) denotes the (zero)-field-cooled $\chi(T)$ experiment.
$M(H)$ ($H = 0$; $T = 5$ K) is the extrapolated moment to $H = 0$ in the $M(H)$ measurement at $T = 5$ K (see text). ⟨Mn–O–Mo⟩ is the average Mn–O–Mo angle.
[a] $H = 80$ Oe for $CaLaMnMoO_6$.

magnetic frustration mechanism, it appears that the larger the crystallographic distortion, the weaker is the NN superexchange interaction. However, this is not so for the 90° NNN superexchange path [5,23], and we may postulate that for $A = \mathrm{Ba}$, the least distorted compound, the NN superexchange interactions are slightly stronger than their NNN counterparts, whereas the opposite occurs for $A = \mathrm{Ca}$. Finally, for $A = \mathrm{Sr}$, the NN–NNN interactions are of the closest strength, driving the largest magnetic frustration. This argument will be further pursued, with neutron diffraction and magnetic studies of $Ca_{1-x}Ba_x LaMnMoO_6$ solid solutions.

Acknowledgments

The authors are grateful to Dr. M.V. Lobanov, Dr. B. Toby and Dr. G. Popov for helpful discussions. The neutron diffraction data was collected at NIST. This work was supported by the National Science Foundation-Solid State Chemistry Grant DMR-0233697.

References

[1] K.-I. Kobayashi, T. Kimura, H. Sawada, K. Terakura, Y. Tokura, Nature 395 (1998) 677.
[2] K.-I. Kobayashi, T. Kimura, Y. Tomioka, H. Sawada, K. Terakura, Y. Tokura, Phys. Rev. B 59 (1999) 11159.
[3] A. Muñoz, J.A. Alonso, M.T. Casais, M.J. Martínez-Lope, M.T. Fernández-Díaz, J. Phys.: Condens. Matter 14 (2002) 8817.
[4] G. Popov, M. Greenblatt, M. Croft, Phys. Rev. B 67 (2003) 024406.
[5] E.N. Caspi, J.D. Jorgensen, M.V. Lobanov, M. Greenblatt, Phys. Rev. B 67 (2003) 134431.
[6] S. Li, M. Greenblatt, J. Alloys Compounds 338 (2002) 121.
[7] T. Nakamura, J.-H. Choy, J. Solid State Chem. 20 (1977) 233.
[8] T. Horikubi, N. Kamegashira, J. Alloys Compounds 287 (1999) 62.
[9] J.R. Carvajal, Physica B 192 (1993) 55.
[10] A.C. Larson, R.B. von Dreele, Los Alamos National Laboratory, LAUR 86-748, 2004.
[11] B.H. Toby, J. Appl. Crystallogr. 34 (2001) 210.
[12] Q. Lin, M. Greenblatt, M. Croft, J. Solid State Chem. 178 (2005) 1356.
[13] E. Prince, Mathematical Techniques in Crystallography and Materials Science, Springer, New York, 1982.
[14] P.M. Woodward, Acta Crystallogr. B 53 (1997) 32.
[15] R.D. Shannon, Acta Crystallogr. A 32 (1976) 751.
[16] W.L. Roth, Phys. Rev. 110 (1958) 1333.
[17] I.A. Blech, B.L. Averbach, Phys. Rev. 142 (1966) 287.
[18] A. Renninger, S.C. Moss, B.L. Averbach, Phys. Rev. 147 (1966) 418.
[19] S. Chikazumi, Physics of Ferromagnetism, Oxford, New York, 1997, pp. 134–148.
[20] E.N. Caspi, M. Avdeev, S. Short, J.D. Jorgensen, B. Dabrowski, O. Chmaissem, J. Mais, S. Kolesnik, J. Solid State Chem. 177 (2004) 1456.
[21] K. Yoshii, J. Solid State Chem. 151 (2000) 294.
[22] S.H. Kim, P.D. Battle, J. Magn. Magn. Mater. 123 (1993) 273.
[23] G. Blasse, Philips Res. Rep. 20 (1965) 327.